What can facial mechanoreceptors tell the mouse brain about whisking?

Kyle S. Severson[1], Duo Xu[1], Hongdian Yang[1,2], Daniel H. O'Connor[1,*]

[1]The Solomon H. Snyder Department of Neuroscience, Kavli Neuroscience Discovery Institute, Brain Science Institute, The Johns Hopkins University School of Medicine, Baltimore, MD 21205, USA

[2]Current address: Department of Molecular, Cell and Systems Biology, University of California, Riverside, Riverside, CA 92521, USA

*Correspondence: dan.oconnor@jhmi.edu

Abstract

Haptic perception synthesizes touch with proprioception, or sense of body position. Humans and mice alike experience rich active touch of the face. Because most facial muscles lack proprioceptor endings, the sensory basis of facial proprioception remains unsolved. Facial proprioception may instead rely on mechanoreceptors that encode both touch and self-motion. In rodents, whisker mechanoreceptors provide a signal that informs the brain about whisker position. Whisking involves coordinated orofacial movements, so mechanoreceptors innervating facial regions other than whiskers could also provide information about whisking. To define all sources of sensory information about whisking available to the brain, we recorded spikes from mechanoreceptors innervating diverse parts of the face. Whisker motion was encoded best by whisker mechanoreceptors, but also by those innervating whisker pad hairy skin and supraorbital vibrissae. Redundant self-motion responses may provide the brain with a stable proprioceptive signal despite mechanical perturbations such as whisker growth and active touch.

Introduction

Proprioception is the sense of where the body or its parts are in space. To interpret touch, it is critical that the brain also knows where in space the touched body part was at the time of contact. Thus, touch and proprioception are intimately linked during normal sensory-motor function. Touch begins with the activation of low-threshold mechanoreceptors (LTMRs) in the skin. Information about body position can come from efference copy signals that report the motor commands ultimately used to control muscles. However, the nervous system contains dedicated mechanoreceptive proprioceptor endings to provide feedback about actual, rather than intended, position. Classical proprioceptors include muscle spindle and Golgi tendon organ afferents.

Many rodents use rapid motions of their mystacial vibrissae (whiskers) to explore the tactile world (Carvell and Simons, 1990; Welker, 1964; Wineski, 1983). Curiously, the muscles controlling these “whisking” motions, as with other facial muscles, lack classical proprioceptor endings (Moore et al., 2015). Therefore, feedback about whisker position must occur via self-motion-triggered (“reafferent”) activity of peripheral mechanoreceptors other than classical muscle proprioceptors, such as the cutaneous LTMRs responsible for sensing touch. Neurons throughout the whisker somatosensory system respond to whisker self-motion in a manner that depends on the relative position of the whisker within the current whisk cycle, or whisk “phase” (Campagner et al., 2016; Crochet and Petersen, 2006; Curtis and Kleinfeld, 2009; Fee et al., 1997; Hires et al., 2015; Khatri et al., 2009; Leiser and Moxon, 2007; Moore et al., 2015; Severson et al., 2017; Wallach et al., 2016; Yu et al., 2006; Yu et al., 2016). Whisk phase is thought to be a key coordinate system for whisker-based sensation (Curtis and Kleinfeld, 2009; Kleinfeld and Deschenes, 2011; Szwed et al., 2003).

LTMRs that innervate the whisker follicles encode whisk phase and other aspects of whisker motion and touch during active sensing (Bush et al., 2016; Campagner et al., 2016; Khatri et al., 2009; Leiser and Moxon, 2007; Severson et al., 2017; Szwed et al., 2003; Szwed

et al., 2006; Wallach et al., 2016). These LTMRs include Merkel-type endings, which are slowly adapting and thought to play a major role in perception of object shape and texture. Individual Merkel and unidentified slowly adapting whisker afferents respond both to touch and to self-motion (Severson et al., 2017). Self-motion (reafferent) responses arise from diverse mechanical sensitivities of whisker afferents (Campagner et al., 2016; Severson et al., 2017; Wallach et al., 2016), and may be used by the brain for whisker proprioception (for behavioral studies addressing whisker proprioception, see: Knutsen et al., 2006; Mehta et al., 2007; O'Connor et al., 2013). Neurons in the brainstem (one synapse downstream from mechanoreceptors) with tactile receptive fields on parts of the face other than whiskers can also respond during whisking in a manner that reports whisk phase (Moore et al., 2015). This suggests that mechanoreceptors innervating facial parts other than whiskers could encode whisker motion, including whisk phase, but this has not been tested. What is the full set of possible mechanoreceptor sources of information that could tell the mouse brain about whisker motion, and how do they compare to one another?

Here, we addressed this question by recording whisker motion and electrophysiological responses from primary mechanoreceptor afferents innervating several distinct structures on the face, including regions of hairy skin, vibrissae other than the mystacial whiskers, and jaw muscles (Figure 1A). We compared the encoding of whisker motion among these different populations of mechanoreceptors to that of whisker mechanoreceptors. We find that a subset of hairy skin mechanoreceptors encodes whisker motion at levels comparable to whisker mechanoreceptors. However, as a population, whisker and other non-whisker vibrissae mechanoreceptors encode the most information about whisker motion. Our results suggest that information about whisking arises from multiple sensory sources, providing the brain with a robust basis for facial proprioception.

Results

Self-motion encoding by whisker mechanoreceptors

We obtained electrophysiological and high-speed video recordings (500 Hz) from head-fixed mice as they ran on a treadmill and whisked freely in air (Figure 1B; Supplemental Video 1). From these video frames, we measured several kinematic variables derived from the whisker's angular position (θ) (Figure 1C). During whisking θ can be decomposed into three quantities that the brain appears to process differently (Hill et al., 2011): midpoint (θ_{mid}), amplitude (θ_{amp}), and phase (Φ) (Figure 1D; Materials and Methods). Whisker primary motor cortex (wM1) robustly encodes θ_{mid} and θ_{amp} (Hill et al., 2011; Huber et al., 2012), and sends this information along cortico-cortical pathways to primary somatosensory cortex (wS1) (Petreanu et al., 2012). This suggests that the brain could use efference copy to keep track of θ_{mid} and θ_{amp}. A small fraction of neurons in wM1 does encode Φ, including after transection of the infraorbital nerve (Hill et al., 2011) that carries sensory information from the whisker pad (Dorfl, 1985). However, the encoding of Φ by neurons across all levels of the ascending somatosensory system, as well as the elimination of phase signals in wS1 after peripheral block of whisking (Fee et al., 1997), indicate a major reafferent contribution to phase coding in the brain. For this reason, and because whisk phase is thought to be a key coordinate scheme for whisker sensation, we focused analysis of the encoding of whisk phase. However, we also analyzed encoding of θ_{mid} and θ_{amp} to determine whether they too could be directly sensed, and encoding of whisker angle (θ), angular velocity (θ'), and angular acceleration (θ''), as these quantities give insight into the mechanical basis of what makes mechanoreceptors spike (Severson et al., 2017; Wallach et al., 2016). We aligned these kinematic quantities with simultaneously recorded spikes from different classes of facial mechanoreceptor afferents (Figure 1E).

We first analyzed units in the trigeminal ganglion (TG) with touch receptive fields confined to single whiskers (Figure 2A, n = 67). Many of these afferents were direction-selective, preferring manual deflections in either the protraction or retraction direction (not shown). A subset of these whisker afferents was more active during whisking (n = 42 "whisking-

sensitive" units, defined in Glossary) and strongly modulated by phase, preferring to fire at a particular phase of the whisk cycle (Figure 2B,C). This sharp phase tuning largely reflects sensitivity to inertial stresses (Severson et al., 2017). We used information theory analyses to quantify how well spiking of single mechanoreceptors encoded phase and other variables related to whisker kinematics. Specifically, we calculated the mutual information (MI; Cover and Thomas, 2006), a measure of association between two random variables derived from their joint probability distribution (Figure 2D), between (1) spike counts obtained during 2 ms video frames, and (2) binned values (Materials and Methods) of kinematic variables extracted from the video frames, including θ, θ', θ'', θ_{amp}, θ_{mid}, and Φ. Mutual information between phase and spike count for whisker afferents, expressed as a rate via multiplying by the 500 Hz sampling frequency, was 9.1 ± 23.8 bits/s (median ± interquartile range [IQR]; n = 42 whisking-sensitive units). To determine which kinematic variable best accounted for the spiking of whisker afferents, we calculated a "normalized mutual information" by dividing MI by the spike count entropy (Jamali et al., 2016). This quantity gives the fraction of spike count uncertainty accounted for by a given kinematic variable. Whisker afferent spike counts were better explained by phase (Figure 2E; normalized MI = 0.096 ± 0.121; median ± IQR) than by θ (0.034 ± 0.064), θ' (0.046 ± 0.086), θ'' (0.030 ± 0.076), θ_{amp} (0.012 ± 0.024), or θ_{mid} (0.0089 ± 0.013; $p < 0.0031$ for all 5 comparisons, two-tailed K-S tests).

Whisker motion coding by mechanoreceptors innervating hairy skin

While whisker mechanoreceptors showed strong phase coding, our goal was to put this coding into context by comparing the information provided by these whisker afferents to that of any other types of mechanoreceptor we could find that responded during whisking in air. We began by recording from TG units with touch receptive fields on hairy skin (n = 85) rather than a vibrissa (Figure 3A). Afferents responded to manual deflections of all small hairs or a small number of guard hairs within the mapped receptive field, were rapidly adapting, and responded

to touch in all directions (not shown). Remarkably, activity of a large number of facial hairy skin afferents was modulated during whisking in air (Figure 3B, 58 of 85 were whisking-sensitive). Consistent with the lack of direction-selectivity, many facial hairy skin afferents fired at multiple phases (e.g. both protraction and retraction phases) of the whisk cycle (Figure 3C). Phase coding by hairy skin afferents varied by receptive field location, such that units with receptive fields closer to the whisker pad tended to encode phase more strongly than those distant from the pad (Figure 3D; overall MI rate = 1.3 ± 4.5 bits/s; median ± IQR).

We next grouped the hairy skin receptive fields into six different "zones" of the face (Figure S1), including the pad, cheek, snout, eye, lip, and jaw. Units with receptive fields on the whisker pad (n = 14) were particularly modulated by phase (13 of 14 were whisking-sensitive). We found several receptive fields comprised of small hairs surrounding whisker follicles, in between whisker arcs or rows, or flanking the outer whiskers. Receptive fields on the pad were smaller in area than other regions of the face (Figure 3D). Pad hairy skin afferent encoding of phase (MI rate = 9.26 ± 8.53 bits/s, median ± IQR) was comparable to whisker afferents and significantly higher than afferents innervating hairy skin on the cheek (0.73 ± 2.10 bits/s), eye (1.11 ± 3.57 bits/s), lip (0.75 ± 1.76 bits/s), snout (1.63 ± 1.23 bits/s), and jaw (0.08 ± 0.09 bits/s; Figure 3E, $p < 0.032$ for all 5 two-tailed K-S tests). Across all facial hairy skin afferents, normalized MI (Figure 3F) was significantly higher for phase (0.0165 ± 0.0348) compared to θ' (0.0062 ± 0.0098), θ'' (0.0056 ± 0.0098), θ_{amp} (0.0085 ± 0.012), and θ_{mid} (0.0094 ± 0.011; $p<0.003$ for all 4 two-tailed K-S tests), but similar to θ (0.014 ± 0.023; $p = 0.77$ two-tailed K-S test).

Video capturing facial motion and whisker position suggested that widespread patterns of skin strain likely occur in a manner correlated with whisking, with stronger correlations between skin and whisker displacements occurring for facial regions on or near the whisker pad (Supplementary Video 2; Figure S1). In addition to skin movements, we observed that the

vibrissae above the eye whisk in phase with the whiskers. We next focused our attention on vibrissae outside of the whisker pad.

Non-mystacial vibrissa movement correlates with whisking

Mice have several vibrissae outside of the mystacial pad, including two supraorbital vibrissae above the eye, one genal vibrissa on the cheek (Danforth, 1925), and several microvibrissae on the upper lip (Figure 4A; Brecht et al., 1997). These sinus follicle structures are highly conserved within strains of mice (Dun and Fraser, 1958) and are present in many other mammals (Danforth, 1925; Wineski, 1983). Surprisingly, in our high-speed videos we noticed periodic movement of supraorbital vibrissae apparently locked to whisking (Supplementary Video 2). To quantify these movements we simultaneously tracked non-mystacial vibrissae and whiskers (i.e. mystacial vibrissae) using high-speed videography. Supraorbital vibrissae (Figure 4B-D; Supplemental Video 3) and the genal vibrissa (Figure 4B-D, Supplemental Video 4) moved in phase with the whiskers. We observed some instances of “missed” whisk cycles, in which the whisker moved, but the supraorbital or genal vibrissae remained still (Figure S2). Microvibrissa barely moved (Figure 4B-D; Supplemental Video 5). Small translations we observed could be due to passive pulling of lip tissue during whisking, rather than active rotation of the microvibrissa follicle.

We computed cross-correlations to quantify the phase lag and degree of correlation between whiskers and the supraorbital and genal vibrissae, and microvibrissae (Figure 4E). We first analyzed pairs of mystacial whiskers to set an “upper bound” on correlations, as whiskers in the same row have highly correlated movements (Wallach et al., 2016). Adjacent whiskers correlated almost perfectly (Pearson’s correlation coefficient, $r = 0.98 \pm 0.03$, n = 14 recordings from 11 mice) with no phase lag (0.00 ± 0.03 radians). These strong correlations among whiskers also validated the use of adjacent or nearby whiskers—chosen for their convenience in

obtaining high-speed videos of both whiskers and other vibrissae—when quantifying correlations between whiskers and other vibrissae.

Supraorbital vibrissae movements correlated strongly with whisker movements (r = 0.78 ± 0.07, mean ± SD, n = 6 recordings from 6 mice), but with a short delay (Figure 4B,E; Φ_{lag} = 0.27 ± 0.05 radians, mean ± SD; p = 4.9e-12, one-tailed t-test). Whisking amplitude (θ_{amp}) was smaller for supraorbital vibrissae (4.7 ± 2.1°, mean ± SEM) compared to whiskers (Figure 4F; 12.5 ± 2.5°, mean ± SEM; p = 1.1e-6, one-tailed t-test).

Genal vibrissa motion also correlated strongly with that of the whiskers (r = 0.83 ± 0.08, mean ± SD), but with a longer phase delay (Figure 4C,E; Φ_{lag} = 0.61 ± 0.18 radians, mean ± SD; p = 9.9e-11, one-tailed t-test). Whisking amplitude for genal vibrissae was also smaller (2.2 ± 1.4°, mean ± SEM) compared to the tracked whiskers (Figure 4F; p = 6.9e-9, one-tailed t-test) and supraorbital vibrissae (p = 0.016, one-tailed t-test).

Microvibrissae motion correlated with whisker motion less well (r = 0.27 ± 0.29, mean ± SD, n = 3 recordings from 3 mice) with a short delay (Φ_{lag} = 0.44 ± 0.11 radians, mean ± SD; p = 4.8e-10, one-tailed t-test; Figure 4D,E). Whisking amplitude for microvibrissae (Figure 4F, 0.84 ± 0.23°, mean ± SEM) was smaller than for whiskers (p = 3.5e-7, one-tailed t-test) and supraorbital vibrissae (p = 0.0086, one-tailed t-test). With smaller amplitude movements and smaller sizes, the mechanical stresses generated at the base of microvibrissae during whisking are likely smaller than those at the bases of other vibrissae types.

Non-mystacial vibrissa mechanoreceptors encode information about whisking

The motion of non-mystacial vibrissae was correlated with whisker motion during whisking. Therefore mechanoreceptors with receptive fields on these vibrissae could show activity patterns that encode whisker self-motion. To test this possibility, we recorded from TG units with touch receptive fields on non-mystacial vibrissae. We found units, some of which were active during whisking, on supraorbital vibrissae (8 of 17 whisking-sensitive), genal vibrissae (3 of 8

whisking-sensitive), and microvibrissae (8 of 10 whisking-sensitive). Non-mystacial vibrissa afferent spiking aligned with whisk phase (Figure 4G). Similar to whisker afferents, we observed examples of sharp phase tuning (Figure 4H).

Supraorbital afferents encoded similar amounts of information about phase (MI rate = 16.2 ± 14.9 bits/s, median ± IQR) as genal afferents (5.2 ± 8.6 bits/s, median ± IQR; $p = 0.23$, two-tailed K-S test), and more than microvibrissa afferents (Figure 4I; 0.74 ± 1.60 bits/s, median ± IQR; $p = 0.0014$, two-tailed K-S test). The spike counts of non-mystacial vibrissa afferents overall were better explained by Φ (Figure 4J; normalized MI = 0.062 ± 0.17, median ± IQR) and θ (0.047 ± 0.042) compared to θ_{amp} (0.019 ± 0.034), and θ_{mid} (0.021 ± 0.033; $p < 0.049$ for all 4 two-tailed K-S tests).

Information encoded by jaw proprioceptors

The trigeminal mesencephalic nucleus (MeV) resides in the brainstem and contains mechanoreceptor neurons that innervate the masseter muscles involved in mastication. Recently, it has been suggested that MeV neurons respond to aspects of whisker motion (Mameli et al., 2017; Mameli et al., 2010; Mameli et al., 2014), which necessitates their inclusion in a full account of possible sources of peripheral information about whisker motion available to the brain (Bosman et al., 2011). We thus recorded the activity of single neurons using 32-channel tetrode microdrives implanted in MeV (Figure 5A).

As with TG recordings, head-fixed mice were placed on a treadmill to elicit running and whisking. Mice also licked at a lickport for water rewards. We used this preparation to identify jaw muscle proprioceptors, as their activity was strongly modulated by the licking associated with reward consumption (Figure 5B,C). For analysis we considered both these putative jaw muscle proprioceptors (n = 23 units), plus units that were recorded on the same tetrode as a putative proprioceptor (n = 20 units) and therefore also presumably in MeV. We did not observe obvious phasic modulation of MeV activity during whisking (Figure 5B; periods of licking

excluded from this analysis). MeV units (n = 33 whisking-sensitive) were not tuned to whisk phase (Figure 5D) and thus did not encode much information about phase (0.04 ± 0.04 bits/s, median ± IQR).

However, we did observe a correlation between MeV activity and whisking midpoint (Figure 5D,E). Several units increased or decreased spiking with increasing θ_{mid}. In addition, the kinematic variables that associated best with MeV spike counts were midpoint, amplitude, and position (Figure 5F). However, MI values between spike count and these quantities were low (e.g. θ_{mid}: 0.17 ± 0.38 bits/s, median ± IQR). Thus, MeV activity is not correlated with whisk phase and appears only weakly correlated with whisking midpoint. We speculate that this weak correlation may be explained by slight changes in jaw position associated with whisking around more or less protracted midpoints.

Comparison of whisker motion coding across facial mechanoreceptor classes

So far we have described how well whisker afferents and other types of facial mechanoreceptors encode whisk phase and other variables related to whisker motion. A major goal was to compare whisker self-motion coding by whisker afferents with that of other classes of afferents. We directly compared coding of whisk phase and midpoint, given the importance of these variables in describing whisking behavior and neural activity (Curtis and Kleinfeld, 2009; Hill et al., 2011; Kleinfeld and Deschenes, 2011; Severson et al., 2017; Wallach et al., 2016). Overall, as a population the non-mystacial vibrissae afferents best encoded θ_{mid} (Figure 6A; MI rate = 0.81 ± 1.80 bits/s, median ± IQR), with similar encoding by whisker afferents (0.68 ± 1.08 bits/s, median ± IQR; p = 0.28 two-tailed K-S test vs non-mystacial afferents) and facial hairy skin afferents (0.72 ± 1.16 bits/s, median ± IQR; p = 0.61 two-tailed K-S test). MeV spike counts encoded θ_{mid} less well than all other afferent classes (0.17 ± 0.38 bits/s, median ± IQR; p < 6.7e-4 for all three two-tailed K-S tests). Similarly, normalized mutual information values showed that θ_{mid} explained spike counts less well for MeV than for all other afferent classes (Figure 6B;

MeV: 0.0019 ± 0.0077; whiskers: 0.0089 ± 0.0134; non-mystacial vibrissae: 0.021 ± 0.033; facial hairy skin: 0.0094 ± 0.0110; median ± IQR; $p < 6.2e-4$ for all three two-tailed K-S tests of MeV vs other afferents).

Phase was best encoded by whisker (Figure 6C; MI rate = 9.1 ± 23.8 bits/s, median ± IQR) and non-mystacial vibrissae afferents (2.9 ± 11.9 bits/s, median ± IQR; $p = 0.15$ two-tailed K-S test vs whisker) compared with facial hairy skin afferents (1.3 ± 4.5 bits/s, median ± IQR; $p = 3.0e-5$, two-tailed K-S test vs whisker) and MeV afferents (0.04 ± 0.04 bits/s, median ± IQR; $p = 8.9e-16$, two-tailed K-S test vs whisker). Similarly, normalized mutual information values showed that phase better explained the spike count of whisker afferents (Figure 6D; 0.096 ± 0.121, median ± IQR) compared with facial hairy skin (0.017 ± 0.035, median ± IQR; $p = 1.0e-10$, two-tailed K-S test), non-mystacial vibrissae (0.062 ± 0.166, median ± IQR; $p = 0.02$, two-tailed K-S test), and MeV afferents (6e-4 ± 10e-4, median ± IQR; $p = 8.9e-17$, two-tailed K-S test).

While whisker mechanoreceptors as a group were overall best at encoding phase, other mechanoreceptor populations included more or less informative subgroups. For a more stringent comparison, we considered the best encoding subgroup from each population: whisker pad mechanoreceptors within facial hairy skin, supraorbital vibrissa mechanoreceptors within non-mystacial vibrissae, and putative jaw muscle proprioceptors within MeV. Mutual information between phase and spike count was similar for whisker (Figure 6E; $n = 42$; 9.1 ± 23.8 bits/s), pad ($n = 13$; 9.3 ± 8.5 bits/s, median ± IQR), and supraorbital mechanoreceptors ($n = 8$; 16.2 ± 14.9 bits/s; $p > 0.11$ for all three two-tailed K-S tests), and negligible for jaw proprioceptors ($n = 23$; 0.04 ± 0.04 bits/s; $p < 8.4e-6$ for all three two-tailed K-S tests). Thus, while whisker mechanoreceptors as a group best encode whisk phase, mechanoreceptors with receptive fields on whisker pad hairy skin and on the supraorbital vibrissae also send to the brain a signal that encodes whisk phase (Figure 6F).

Discussion

Here we surveyed primary mechanoreceptive afferents that innervate multiple regions of the face to quantify correlations between spiking activity of these mechanoreceptors and whisker motion. Our specific goal was to provide a comprehensive account of the possible sources of reafferent information sent to the brain about whisking. This quantitative survey provides important context to interpret the encoding of whisker motion—and in particular, whisk phase—previously observed among whisker afferents (Campagner et al., 2016; Severson et al., 2017; Wallach et al., 2016), and more generally to investigate the hypothesis that facial proprioception relies on the reafferent activity of cutaneous LTMRs. We found that whisker afferents as a group encoded whisk phase best, together with supraorbital and genal vibrissae afferents. Thus, our results support the hypothesis that the strong phase coding observed in prior work with whisker afferents (Campagner et al., 2016; Severson et al., 2017; Wallach et al., 2016) could serve as a basis for whisker proprioception.

We found that a large number of mechanoreceptors with receptive fields on the hairy skin of the face responded in a phasic manner during whisking. While passive or active touch of the whiskers did not strongly activate facial hairy skin mechanoreceptors, passive stretch of the skin within or near their receptive fields was sufficient to cause spiking (not shown). This suggests that skin strain occurring within the receptive field, and in a pattern correlated with whisker motion, likely underlies the self-motion responses of these afferents. Activity of cutaneous afferents has also been reported during jaw movements in rabbits, with activity of non-direction selective, hairy skin afferents responding to self-motion in a manner proportional to movement speed (Appenteng et al., 1982). In humans, microneurography studies have reported activity in cutaneous afferents related to active movement of the face (Johansson et al., 1988), ankle (Aimonetti et al., 2007), knee (Edin, 2001), and finger (Edin and Abbs, 1991; Hulliger et al., 1979). Thus, “cutaneous” (reafferent) signals of potential use for proprioception occur across a wide variety of body parts and animal species.

Using high-speed videography, we found correlated motions of the non-mystacial vibrissae and the mystacial whiskers. In rodents, major aspects of the structure and innervation (Fundin et al., 1995; Wineski, 1985) of the supraorbital and genal vibrissae closely resemble those of mystacial vibrissae (Fundin et al., 1994). Motions of these non-mystacial vibrissae were assessed in the golden hamster, and they were found to be relatively immobile (Wineski, 1983). Here, we show that in mice, supraorbital and genal vibrissae are indeed mobile and whisk in phase with the whiskers. The observation of tight coupling of whisker and non-mystacial vibrissa movements adds to our understanding of the exquisitely coordinated orofacial motor actions in rodents (Kurnikova et al., 2017; Welker, 1964) and suggests that their premotor circuits are linked (Deschenes et al., 2016; Kleinfeld et al., 2014; McElvain et al., 2018; Moore et al., 2013). Afferents with receptive fields on these structures, especially the supraorbital and genal vibrissae, displayed strong phase tuning and carried information about phase comparable to that of whisker afferents. While these afferents encode the phase of the whiskers in the whisk cycle, the supraorbital and genal vibrissae are unlikely to contact objects that are in reach of the whiskers. Thus, an interesting possibility is that afferents with these non-whisker vibrissae receptive fields could provide the brain with a phase signal that is, unlike that of the whisker afferents we report here and in past work (Severson et al., 2017), unperturbed by contacts between whiskers and objects in the world. Alternatively, whisker afferents that respond to whisking in air but not touch have also been found and could serve this role (Szwed et al., 2003). Neural circuits that separate touch and self-motion signals arising from the same neurons are also possible (Moore et al., 2015).

Recent reports have found that neurons in the trigeminal mesencephalic nucleus can be activated during periods of whisker motion, leading to the suggestion that MeV neurons encode whisking kinematics (Mameli et al., 2017; Mameli et al., 2010; Mameli et al., 2014). However, these studies were limited to anesthetized animals. To clarify whether MeV must be considered as a source of information about whisking kinematics (Bosman et al., 2011) during behavior, we

recorded extracellularly from MeV units during periods of active whisking and during periods of licking. We found that MeV units did not encode whisk phase nor other rapid aspects of whisker motion. MeV units did encode the midpoint of whisking, albeit very modestly relative to other afferent classes. MeV houses the muscle spindles of jaw muscles, which spike during jaw movements (Goodwin and Luschei, 1975). We therefore speculate that these weak correlations with midpoint occur due to coordinated motion of the jaw and whisker pad, perhaps with subtle jaw muscle changes occurring at more protracted whisking midpoints (which occur at higher locomotion speeds; Sofroniew et al., 2014). However, we identified MeV units in our extracellular recordings based on responses to licking (presumably jaw-motion-correlated), or based on a unit being recorded on the same tetrode (nearby location) as a licking-correlated unit. It is possible that MeV houses neurons that we did not sample and that encode other aspects of whisking.

Together, our results provide a quantitative survey of how much information mechanoreceptors in the face can provide the mouse brain about whisking. Our data reveal that non-mystacial vibrissae can whisk in phase with the whiskers, and that mechanoreceptors innervating these non-mystacial vibrissae, as well as a subset of mechanoreceptors innervating facial hairy skin, can provide the brain with information about whisker motion comparable to mechanoreceptors that innervate the whiskers. Whisker mechanoreceptors provided the best, but not the only, source of information about whisking for the brain to use in whisker proprioception. We conclude that the coding of whisker self-motion occurs via a multitude of sensory signals arising from distinct classes of facial mechanoreceptors.

Author Contributions

KSS and HY performed experiments. KSS and DX developed analysis code. KSS analyzed data. KSS and DHO wrote the paper with input from all authors.

Acknowledgements

We thank Ernst Niebur for discussion of data analysis and Bilal Bari for demonstration of MeV recording. We thank Ernst Niebur, Kathleen Cullen, Jeremiah Cohen and William Olson for comments on the manuscript. The authors were supported by NIH grants R01NS089652 and 1R01NS104834-01.

References

Aimonetti, J.M., Hospod, V., Roll, J.P., and Ribot-Ciscar, E. (2007). Cutaneous afferents provide a neuronal population vector that encodes the orientation of human ankle movements. J Physiol *580*, 649-658.

Appenteng, K., Lund, J.P., and Seguin, J.J. (1982). Behavior of cutaneous mechanoreceptors recorded in mandibular division of Gasserian ganglion of the rabbit during movements of lower jaw. J Neurophysiol *47*, 151-166.

Bosman, L.W., Houweling, A.R., Owens, C.B., Tanke, N., Shevchouk, O.T., Rahmati, N., Teunissen, W.H., Ju, C., Gong, W., Koekkoek, S.K.*, et al.* (2011). Anatomical pathways involved in generating and sensing rhythmic whisker movements. Front Integr Neurosci *5*, 53.

Brecht, M., Preilowski, B., and Merzenich, M.M. (1997). Functional architecture of the mystacial vibrissae. Behav Brain Res *84*, 81-97.

Bush, N.E., Schroeder, C.L., Hobbs, J.A., Yang, A.E., Huet, L.A., Solla, S.A., and Hartmann, M.J. (2016). Decoupling kinematics and mechanics reveals coding properties of trigeminal ganglion neurons in the rat vibrissal system. Elife *5*.

Campagner, D., Evans, M.H., Bale, M.R., Erskine, A., and Petersen, R.S. (2016). Prediction of primary somatosensory neuron activity during active tactile exploration. Elife *5*.

Carvell, G.E., and Simons, D.J. (1990). Biometric analyses of vibrissal tactile discrimination in the rat. J Neurosci *10*, 2638-2648.

Clack, N.G., O'Connor, D.H., Huber, D., Petreanu, L., Hires, A., Peron, S., Svoboda, K., and Myers, E.W. (2012). Automated tracking of whiskers in videos of head fixed rodents. PLoS Comput Biol *8*, e1002591.

Cohen, J.Y., Haesler, S., Vong, L., Lowell, B.B., and Uchida, N. (2012). Neuron-type-specific signals for reward and punishment in the ventral tegmental area. Nature *482*, 85-88.

Cover, T.M., and Thomas, J.A. (2006). Elements of information theory, 2nd edn (Hoboken, N.J.: Wiley-Interscience).

Crochet, S., and Petersen, C.C. (2006). Correlating whisker behavior with membrane potential in barrel cortex of awake mice. Nat Neurosci *9*, 608-610.

Curtis, J.C., and Kleinfeld, D. (2009). Phase-to-rate transformations encode touch in cortical neurons of a scanning sensorimotor system. Nat Neurosci *12*, 492-501.

Danforth, C.H. (1925). Hair in its relation to questions of homology and phylogeny. American Journal of Anatomy *36*, 47-68.

Deschenes, M., Takatoh, J., Kurnikova, A., Moore, J.D., Demers, M., Elbaz, M., Furuta, T., Wang, F., and Kleinfeld, D. (2016). Inhibition, Not Excitation, Drives Rhythmic Whisking. Neuron *90*, 374-387.

Dorfl, J. (1985). The innervation of the mystacial region of the white mouse: A topographical study. J Anat *142*, 173-184.

412 Dun, R.B., and Fraser, A.S. (1958). Selection for an invariant character; vibrissa number in the house
413 mouse. Nature *181*, 1018-1019.
414 Edin, B. (2001). Cutaneous afferents provide information about knee joint movements in humans. J
415 Physiol *531*, 289-297.
416 Edin, B.B., and Abbs, J.H. (1991). Finger movement responses of cutaneous mechanoreceptors in the
417 dorsal skin of the human hand. J Neurophysiol *65*, 657-670.
418 Fee, M.S., Mitra, P.P., and Kleinfeld, D. (1997). Central versus peripheral determinants of patterned
419 spike activity in rat vibrissa cortex during whisking. J Neurophysiol *78*, 1144-1149.
420 Fundin, B.T., Arvidsson, J., and Rice, F.L. (1995). Innervation of nonmystacial vibrissae in the adult rat. J
421 Comp Neurol *357*, 501-512.
422 Fundin, B.T., Rice, F.L., Pfaller, K., and Arvidsson, J. (1994). The innervation of the mystacial pad in the
423 adult rat studied by anterograde transport of HRP conjugates. Exp Brain Res *99*, 233-246.
424 Goodwin, G.M., and Luschei, E.S. (1975). Discharge of spindle afferents from jaw-closing muscles during
425 chewing in alert monkeys. J Neurophysiol *38*, 560-571.
426 Hill, D.N., Curtis, J.C., Moore, J.D., and Kleinfeld, D. (2011). Primary motor cortex reports efferent control
427 of vibrissa motion on multiple timescales. Neuron *72*, 344-356.
428 Hires, S.A., Gutnisky, D.A., Yu, J., O'Connor, D.H., and Svoboda, K. (2015). Low-noise encoding of active
429 touch by layer 4 in the somatosensory cortex. Elife *4*.
430 Huber, D., Gutnisky, D.A., Peron, S., O'Connor, D.H., Wiegert, J.S., Tian, L., Oertner, T.G., Looger, L.L., and
431 Svoboda, K. (2012). Multiple dynamic representations in the motor cortex during sensorimotor learning.
432 Nature *484*, 473-478.
433 Hulliger, M., Nordh, E., Thelin, A.E., and Vallbo, A.B. (1979). The responses of afferent fibres from the
434 glabrous skin of the hand during voluntary finger movements in man. J Physiol *291*, 233-249.
435 Jamali, M., Chacron, M.J., and Cullen, K.E. (2016). Self-motion evokes precise spike timing in the primate
436 vestibular system. Nat Commun *7*, 13229.
437 Johansson, R.S., Trulsson, M., Olsson, K.A., and Abbs, J.H. (1988). Mechanoreceptive afferent activity in
438 the infraorbital nerve in man during speech and chewing movements. Exp Brain Res *72*, 209-214.
439 Khatri, V., Bermejo, R., Brumberg, J.C., Keller, A., and Zeigler, H.P. (2009). Whisking in air: encoding of
440 kinematics by trigeminal ganglion neurons in awake rats. J Neurophysiol *101*, 1836-1846.
441 Kleinfeld, D., and Deschenes, M. (2011). Neuronal basis for object location in the vibrissa scanning
442 sensorimotor system. Neuron *72*, 455-468.
443 Kleinfeld, D., Moore, J.D., Wang, F., and Deschenes, M. (2014). The Brainstem Oscillator for Whisking
444 and the Case for Breathing as the Master Clock for Orofacial Motor Actions. Cold Spring Harb Symp
445 Quant Biol *79*, 29-39.
446 Knutsen, P.M., Pietr, M., and Ahissar, E. (2006). Haptic object localization in the vibrissal system:
447 behavior and performance. J Neurosci *26*, 8451-8464.
448 Kurnikova, A., Moore, J.D., Liao, S.-M., Deschenes, M., and Kleinfeld, D. (2017). Coordination of orofacial
449 motor actions of the nose, head, and vibrissae into exploratory behavior. Curr Biol.
450 Leiser, S.C., and Moxon, K.A. (2007). Responses of trigeminal ganglion neurons during natural whisking
451 behaviors in the awake rat. Neuron *53*, 117-133.
452 Mameli, O., Caria, M.A., Biagi, F., Zedda, M., and Farina, V. (2017). Neurons within the trigeminal
453 mesencephalic nucleus encode for the kinematic parameters of the whisker pad macrovibrissae. Physiol
454 Rep *5*.
455 Mameli, O., Stanzani, S., Mulliri, G., Pellitteri, R., Caria, M.A., Russo, A., and De Riu, P. (2010). Role of the
456 trigeminal mesencephalic nucleus in rat whisker pad proprioception. Behav Brain Funct *6*, 69.
457 Mameli, O., Stanzani, S., Russo, A., Pellitteri, R., Manca, P., De Riu, P.L., and Caria, M.A. (2014).
458 Involvement of trigeminal mesencephalic nucleus in kinetic encoding of whisker movements. Brain Res
459 Bull *102*, 37-45.

460 McElvain, L.E., Friedman, B., Karten, H.J., Svoboda, K., Wang, F., Deschenes, M., and Kleinfeld, D. (2018).
461 Circuits in the rodent brainstem that control whisking in concert with other orofacial motor actions.
462 Neuroscience *368*, 152-170.
463 Mehta, S.B., Whitmer, D., Figueroa, R., Williams, B.A., and Kleinfeld, D. (2007). Active spatial perception
464 in the vibrissa scanning sensorimotor system. PLoS Biol *5*, e15.
465 Moore, J.D., Deschenes, M., Furuta, T., Huber, D., Smear, M.C., Demers, M., and Kleinfeld, D. (2013).
466 Hierarchy of orofacial rhythms revealed through whisking and breathing. Nature *497*, 205-210.
467 Moore, J.D., Mercer Lindsay, N., Deschenes, M., and Kleinfeld, D. (2015). Vibrissa self-motion and touch
468 are reliably encoded along the same somatosensory pathway from brainstem through thalamus. PLoS
469 Biol *13*, e1002253.
470 O'Connor, D.H., Hires, S.A., Guo, Z.V., Li, N., Yu, J., Sun, Q.Q., Huber, D., and Svoboda, K. (2013). Neural
471 coding during active somatosensation revealed using illusory touch. Nat Neurosci *16*, 958-965.
472 Pammer, L., O'Connor, D.H., Hires, S.A., Clack, N.G., Huber, D., Myers, E.W., and Svoboda, K. (2013). The
473 mechanical variables underlying object localization along the axis of the whisker. J Neurosci *33*, 6726-
474 6741.
475 Petreanu, L., Gutnisky, D.A., Huber, D., Xu, N.L., O'Connor, D.H., Tian, L., Looger, L., and Svoboda, K.
476 (2012). Activity in motor-sensory projections reveals distributed coding in somatosensation. Nature *489*,
477 299-303.
478 Severson, K.S., Xu, D., Van de Loo, M., Bai, L., Ginty, D.D., and O'Connor, D.H. (2017). Active Touch and
479 Self-Motion Encoding by Merkel Cell-Associated Afferents. Neuron *94*, 666-676 e669.
480 Sofroniew, N.J., Cohen, J.D., Lee, A.K., and Svoboda, K. (2014). Natural whisker-guided behavior by head-
481 fixed mice in tactile virtual reality. J Neurosci *34*, 9537-9550.
482 Suter, B.A., O'Connor, T., Iyer, V., Petreanu, L.T., Hooks, B.M., Kiritani, T., Svoboda, K., and Shepherd,
483 G.M. (2010). Ephus: multipurpose data acquisition software for neuroscience experiments. Front Neural
484 Circuits *4*, 100.
485 Szwed, M., Bagdasarian, K., and Ahissar, E. (2003). Encoding of vibrissal active touch. Neuron *40*, 621-
486 630.
487 Szwed, M., Bagdasarian, K., Blumenfeld, B., Barak, O., Derdikman, D., and Ahissar, E. (2006). Responses
488 of trigeminal ganglion neurons to the radial distance of contact during active vibrissal touch. J
489 Neurophysiol *95*, 791-802.
490 Wallach, A., Bagdasarian, K., and Ahissar, E. (2016). On-going computation of whisking phase by
491 mechanoreceptors. Nat Neurosci *19*, 487-493.
492 Welker, W.I. (1964). Analysis of Sniffing of the Albino Rat. Behaviour *22*, 223-244.
493 Wineski, L.E. (1983). Movements of the cranial vibrissae in the Golden hamster (*Mesocricetus auratus*). J
494 Zool *200*, 261-280.
495 Wineski, L.E. (1985). Facial morphology and vibrissal movement in the golden hamster. J Morphol *183*,
496 199-217.
497 Yang, H., Kwon, S.E., Severson, K.S., and O'Connor, D.H. (2016). Origins of choice-related activity in
498 mouse somatosensory cortex. Nat Neurosci *19*, 127-134.
499 Yu, C., Derdikman, D., Haidarliu, S., and Ahissar, E. (2006). Parallel thalamic pathways for whisking and
500 touch signals in the rat. PLoS Biol *4*, e124.
501 Yu, J., Gutnisky, D.A., Hires, S.A., and Svoboda, K. (2016). Layer 4 fast-spiking interneurons filter
502 thalamocortical signals during active somatosensation. Nat Neurosci *19*, 1647-1657.

503

504

Supplemental Video Legends

Supplemental Video 1: Whisker mechanoreceptor activity during whisking.
Raw video (slowed 20-fold) showing mouse whiskers during whisking. The tracked γ whisker is indicated with the black overlay, and its angular position (θ) is shown in the trace at bottom. Spike times from a simultaneously recorded afferent responsive to the C2 whisker (third from right) are indicated as black ticks above the θ trace. Audio is the playback of the spike waveform at the corresponding spike time.

Supplemental Video 2: Whisking is accompanied by widespread motion of the face.
Raw video (slowed 20-fold) showing side-view of a mouse face during whisking. All whiskers except the A1 and A2 whiskers and much of the facial fur have been trimmed, for a better view of the skin. The skin moves in complex patterns during whisking.

Supplemental Video 3: Supraorbital vibrissa movement during whisking.
Raw video (slowed 20-fold) showing mouse whiskers (A1 and A2) and supraorbital (SO) vibrissae during whisking. The A1 whisker (black overlay) and caudal SO vibrissa (blue overlay) are tracked. The angular positions of the whisker (θ_{A1}, black trace) and SO vibrissae (θ_{SO}, blue trace) are shown at bottom. The SO vibrissae whisk in phase with the whiskers.

Supplemental Video 4: Genal vibrissa movement during whisking.
Raw video (slowed 20-fold) showing mouse whiskers (C-row) and genal vibrissa moving in free air. The C1 whisker (black overlay) and genal vibrissa (red overlay) are tracked. The angular positions of the whisker (θ_{C1}, black trace) and genal vibrissa (θ_{G}, red trace) are shown at bottom. The genal vibrissa whisks in phase with the whiskers.

Supplemental Video 5: Microvibrissa movement during whisking.
Raw video (slowed 20-fold) showing mouse whiskers (D2 and D3) and microvibrissae during whisking. The D3 whisker (black overlay) and one of the larger, more dorsal and caudal microvibrissae (green overlay) are tracked. The angular positions of the whisker (θ_{D3}, black trace) and microvibrissa (θ_{μ}, green trace) are shown at bottom. The microvibrissa does not whisk.

Materials and Methods

All procedures were in accordance with protocols approved by the Johns Hopkins University Animal Care and Use Committee.

Mice. Mixed background mice were housed singly in a vivarium with reverse light-dark cycle (12 hours each phase). Behavior experiments were conducted during the dark (active) cycle. The sex and line of each mouse used for recordings is detailed in Table S1.

Surgical preparation – TG recordings. Adult mice (6-18 weeks old) were implanted with titanium headcaps (Yang et al., 2016). Prior to electrophysiological recordings, two small openings (0.5 mm anterior-posterior, 2 mm medial-lateral) in the skull were made centered at 0 and 1.0 mm anterior and 1.5 mm lateral to Bregma, with dura left intact. Craniotomies were covered acutely with hemostatic gelatin sponge (VetSpon, Ferrosan Medical Devices) or chronically with silicone elastomer (Kwik-Cast, WPI) followed by a layer of dental acrylic (Jet Repair Acrylic).

Surgical preparation – MeV recordings. Custom microdrives with eight tetrodes (Cohen et al., 2012) were built to make extracellular recordings from MeV neurons. Each tetrode comprised four recording wires (100-300 kΩ). A ~1 mm diameter craniotomy was made (centered at -5.4 mm caudal to bregma, 0.9 mm lateral to midline) for implanting the microdrive to a depth of 2 mm, ~0.5 mm dorsal to MeV. Adult mice (9-18 weeks old) were implanted with a titanium headcap for head-fixation. The microdrive was advanced in steps of ~100 µm each day until reaching MeV, identified by the presence of clear high-frequency firing responses to jaw opening and/or closing. Putative MeV jaw proprioceptors were identified post hoc by clear modulations of spike rate aligned to lick times (Figure 5C).

Behavioral training and apparatus. Mice received 1 ml water per day for ≥ 7 days prior to training. Mice were head-fixed and placed on a linear treadmill to promote whisking, as mice whisk during running. Voluntary bouts of running were encouraged by providing subsequent water rewards via a custom lickport. On training days (2-10 days total), mice were weighed before and after each session to determine the volume of water consumed. If mice consumed < 1 ml, additional water was given to achieve 1 ml total. During recordings, treadmill position was tracked with a custom optical rotary encoder comprised of a 3D printed encoder disk (2 cm diameter, 20 holes) and a commercial photointerrupter (1A51HR, Sharp).

Whisker and other hair trimming. One day prior to electrophysiological recording, non-mystacial hairs on the left side of the face were trimmed short with fine forceps and microdissection scissors (Fine Science Tools), during isoflurane (1.5%) anesthesia. For TG recordings, all whiskers and microvibrissae were trimmed short except β, γ, δ, B1-4, C1-4, and D1-4. For improved tracking of whiskers, we minimized obstruction of the field of view by hairs that were not whiskers intended to be tracked. We did not use chemical hair remover. Fur between the whiskers was manually removed by plucking or trimming. Non-whisker hairs were maintained at this short length by repeating this procedure as necessary. Receptive fields on facial hairy skin were always on fur cut <1 mm by trimming. Whisker and non-mystacial vibrissa afferents were recorded while the vibrissa in the receptive field was at or near its intact length.

Trigeminal ganglion electrophysiology*.* Recordings from TG afferents were performed as described (Severson et al., 2017). Briefly, awake mice were head-fixed and allowed to run on the treadmill. The craniotomy was exposed and covered with PBS. A single tungsten recording electrode (2 MΩ nominal, Parylene coated; WPI) was lowered ~5.5 mm until it reached the TG.

The tissue was allowed to relax at least 10 min to stabilize recordings. An identical reference electrode was lowered to a similar depth or placed outside the craniotomy in the PBS. The differential electrophysiological signal between recording and reference electrodes was amplified 10,000x, bandpass filtered between 300 Hz and 3,000 Hz (DAM80, WPI), and acquired at 20 kHz in 5 second sweeps. Electrophysiology, high-speed video, and other measurements were synchronized by Ephus (Suter et al., 2010) or WaveSurfer (http://wavesurfer.janelia.org) software. A micromanipulator (Sutter Instruments) advanced the recording electrode until a well-isolated unit responsive to manual touch stimulation was encountered. The unit's receptive field, response type (RA or SA), and direction selectivity were manually classified. All whiskers except the row containing the whisker-of-interest and/or surrogate tracking whisker were trimmed short. Small manual movements of the treadmill encouraged the mouse to run and whisk. After recordings, the craniotomy was covered with silicone elastomer and a thin layer of dental acrylic. Spike waveforms were obtained by thresholding high-pass filtered (500 Hz) traces and clustered using MClust-4.1 or MClust-4.4 (AD Redish et al.). A subset of TG whisker afferent recordings is reanalyzed from a previous report (Severson et al., 2017), as detailed in Supplemental Table 1.

MeV electrophysiology. Water was intermittently delivered via a lickport tube placed below the animal's snout. Lick signals were recorded by a custom electrical circuit designed to detect when the tongue contacted the lickport. Lick traces and broadband voltage traces from individual tetrode wires were acquired continuously at 30 kHz (Intan Technologies). Signals were bandpass filtered online between 0.1 Hz and 10 kHz, highpass filtered offline below 500 Hz, and spikes were detected using a threshold of 4-6 standard deviations of the filtered signal. The timestamp of the peak of each detected spike, as well as a 1-ms waveform centered at the peak, were extracted from each channel of the tetrode for spike sorting, and clustered using MClust (AD Redish et al.).

Mapping facial hairy skin receptive fields. The touch receptive fields of TG units were identified with a hand-held probe, while monitoring activity using an audio monitor (Model 3300, A-M Systems). When a whisker receptive field could not be found, the receptive field could often be located after probing hairy skin on the entire face. In these cases, before recording began, the extent of the receptive field was mapped by determining the region of hair and skin in which gentle touch with fine forceps (Dumont AA, tip dimensions 0.4 mm x 0.2 mm; FST, #11210-10) evoked spikes and marked with a fine, water-based color marker (0.3 mm tip, Micro-Line, Platinum Art Supplies). Following the recording, the mouse's head with marked receptive fields and a micro-ruler (Electron Microscopy Sciences, #62096-08) were photographed (13 megapixel camera, LG Stylo 2) from the side, above, and/or below. The receptive fields were then compiled on a template "face map". The template image was drawn by outlining the profile and fiducial marks (e.g. eye, whisker follicles, nostrils) of a side view image of a mouse's face in Adobe Illustrator CS 6 (Adobe Systems). The approximate shape, location, and relative size of each imaged receptive field were mapped onto the template by: outlining the receptive field, locating nearby fiducial marks in the original image, applying a fixed scaling to match receptive field and template image dimensions, and translating to align to fiducial marks in the template image. Using the SVG Interactivity Panel in Illustrator, receptive fields were tagged with unique identifier text and their coordinates exported to a text file subsequently read into MATLAB. Borders of each zone of the face (e.g. pad, cheek) were drawn by outlining and connecting fiducial marks (Figure S1). Receptive fields were designated to the zone in which the center of mass was located.

High-speed videography. Video frames (640 pixels x 480 pixels, 32 µm/pixel) were acquired at 500 Hz using a PhotonFocus DR1-D1312-200-G2-8 camera (90 µs exposure time) and Streampix 5 software (Norpix). Light from a 940 nm LED (Roithner Laser) was passed through a condenser lens (Thorlabs), through the whisker field, reflected off a mirror (Thorlabs), and directed into a 0.25X telecentric lens (Edmund Optics). Ephus or WaveSurfer triggered individual camera frames (5 seconds, 2,500 frames per sweep) synchronized with electrophysiological recordings. To record microvibrissa movement, whiskers were trimmed, except for the D-row whiskers used for tracking whisker movement. The LED was rotated 30° to capture an oblique view of the profile of the mouse's face, thus maximizing the apparent length of the microvibrissae to enable tracking. To record facial and supraorbital vibrissa movements, the mouse's fur was trimmed to <1 mm, as described above. Whiskers and microvibrissae were trimmed to the base, except for the A-row whiskers used for tracking whisker movement. An additional mirror was placed in the light path to capture a side view of the mouse's face.

Video analysis. All whisker tracking was computing using the Janelia Whisker Tracker (Clack et al., 2012). X-Y coordinates of the whisker objects for each frame were computed by tracing the backbone of each whisker at subpixel-resolution. To reduce noise in measurement of θ, we truncated the tracked whisker trace at its intersection with that frame's "facemask", a curve offset from an outline of the face profile. The facemask was drawn for each frame, briefly, by fitting a smoothing spline to the contour of the face and performing several other image processing steps in MATLAB (Severson et al., 2017). The whisker's follicle location was then estimated by extrapolating past the facemask along the angle of the whisker base (Pammer et al., 2013; Severson et al., 2017). A simple "linking" algorithm was used to ensure the same whisker was tracked across frames. Traced objects outside of the expected region of interest, e.g. whisker pad, and outside of the expected length range were excluded. Whisker identity was then determined based on its follicle X-coordinate in either ascending or descending order. Finally, a number of events could render individual videos ineligible for further processing. These events included objects placed in or entering the video frame or grooming behavior. Using a custom GUI, every sweep was inspected to determine if an exclusion event had occurred.

Processing kinematics. We used the Hilbert transform to quantify the instantaneous phase (Φ), amplitude (θ_{amp}) and midpoint (θ_{mid}) of bandpass (8-30 Hz, Butterworth) filtered θ (Hill et al., 2011). Instantaneous whisking frequency (f_{whisk}) was calculated by taking the time derivative of the unwrapped Φ signal. We first smoothed θ with a Savitzky-Golay filter (3rd order, span of 9 frames) and interpolated missing frames when possible. Angular velocity, θ', the time derivative of θ, was calculated using central differences and smoothed with the same Savitzky-Golay filter. Sweeps with more than 2% of frames having missing θ data were excluded. For θ, θ', θ_{amp}, f_{whisk}, θ_{mid}, observations outside of the 0.25 and 99.75 percentiles were excluded. No outlier removal was performed on Φ. We calculated cross-correlation values (MATLAB 'xcorr' with 'coeff' option) on pairs of traces for whiskers and non-mystacial vibrissae (Figure 4E) after converting the sampling intervals from equally spaced time intervals to equally spaced phase intervals, using linear interpolation separately for each whisk cycle. Whisk cycles containing any non-whisking frames were removed. For cross-correlation analysis, we included between 79 and 333 videos for each session, including 195-591 seconds of whisking data.

Tracking facial movement. We acquired epochs of facial movement with high-speed video (500 Hz, 480 pixels x 640 pixels, 32 µm/pixel) to analyze correlations between facial skin movement and whisker kinematics (Figure S1). Two mirrors were placed in the light path to capture a side view of the mouse's face. Facial hair and whiskers were trimmed short except two A-row whiskers for tracking whisker movement. Displacement of each pixel for each frame

was estimated by applying an image registration algorithm (MATLAB "imregdemons" with pyramid level iterations 32, 16, 8, and 4) that aligns each "moving" frame with a "fixed" template frame. First, fixed and moving frames were resized by half on each dimension (to 320 pixels x 240 pixels; MATLAB "imresize" with bicubic smoothing) to reduce compute time and file size. Next, pixel values outside of the face and in the eye were set to zero. Image registration was then applied to every video frame in the session. We then calculated Pearson's correlation coefficients between the time series of x-dimension pixel displacement values (Δx) and whisker position (θ) time series. Y-displacement values were not used for calculating correlations because they could not be estimated as accurately from 2D images, due to substantial out-of-image-plane curvature of the mouse face that varies along the y-dimension. Mean Pearson's *r* values for each facial region (Figure S1E) were obtained by averaging *r* values across all pixels within each facial region. These regions were determined for the fixed template image using fiducial marks as described above.

Data analysis – tuning curves. To calculate tuning curves, kinematic variables were processed by performing outlier removal, restricting observations to whisking periods, and binning into 30 equally spaced bins, unless otherwise noted. Bins with fewer than 25 observations were set to NaN.

Data analysis – mutual information. Mutual information (MI) was calculated between the distributions of spike counts and kinematic variable values across individual 2 ms frames. The distribution of spike counts was $P(X = x), x \in \{0,1,2, \dots n\}$, where *n* is the maximum number of spikes observed during a single 2 ms frame across the duration of the recording. For the recordings presented here, *n* was ≤ 3. For each kinematic variable, *Y*, the distribution $P(Y)$ was estimated after binning *Y* into 16 equally spaced bins ranging from max(*Y*) to min(*Y*) after removing outliers as described above. Uniform count binning of kinematic variables yielded similar results for θ_{mid} and Φ (Supplemental Figure 3). The joint distribution $P(X = x, Y = y)$ was estimated similarly. MI (Cover and Thomas, 2006) was then computed as:

$$MI(X;Y) = \sum_{x \in X, y \in Y} P(x,y) log_2 \frac{P(x,y)}{P(x)P(y)}$$

To obtain the "MI rate", we multiplied MI by the sampling frequency, which was always 500 Hz. To calculate "normalized MI" for each recording, we first calculated the entropy of the spike count distribution:

$$H_X = -\sum_{x \in X} P(x) \log_2 P(x).$$

Normalized MI was then computed as:

$$Normalized\ MI = \frac{MI(X;Y)}{H_X}$$

<u>Glossary:</u>

"Whiskers": macrovibrissae located on the mystacial pad.
"Non-mystacial vibrissae": vibrissae that are not whiskers; includes supraorbital and genal macrovibrissae, and the microvibrissae.
"Whisking" periods**:** Frames with θ_{amp} > 2.5° and f_{whisk} > 1 Hz for the tracked whisker.
"Non-whisking" periods**:** Frames with θ_{amp} < 1° for the tracked whisker.

“Whisking-sensitive”: Applies to a unit with 95% confidence interval (CI) on mean spike rate during whisking in air non-overlapping with 95% CI for mean spike rate during non-whisking and with mean spike rate > 1 Hz during whisking.

“Whisker afferents” or **“whisker mechanoreceptors”**: LTMRs with single-whisker receptive fields, presumably which innervate the whisker follicle.

“Proprioceptors”: Mechanoreceptors presumed to associate with muscle spindle or Golgi tendon organ structures.

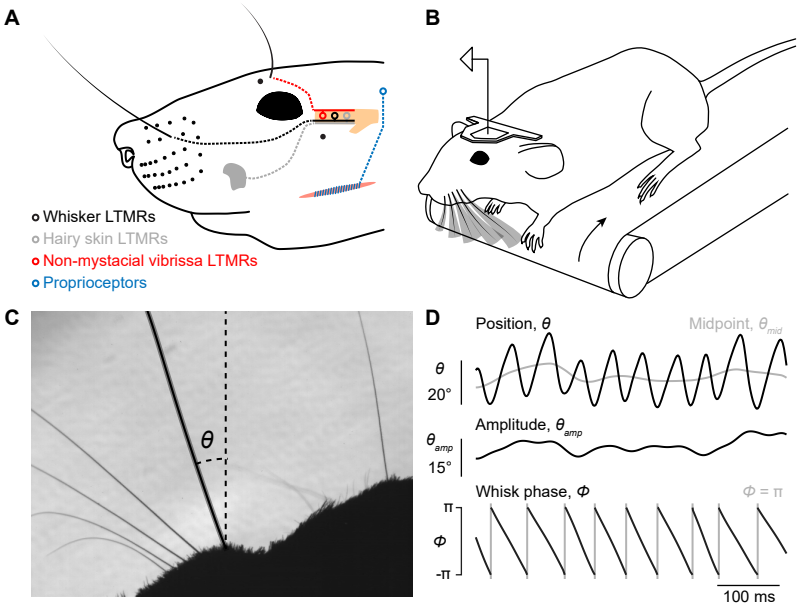

E

Afferent group	Recording location	Units recorded	Units whisking-sensitive
Whisker	TG	67	42
Hairy skin	TG	85	58
Non-mystacial vibrissa	TG	35	19
Proprioceptors	MeV	43	33

Figure 1. Recording whisking and spikes from mechanosensory afferents.
(**A**) Schematic of experimental setup. A head-fixed mouse ran on a treadmill and whisked in air. Single neurons were recorded simultaneously with high-speed (500 Hz) video of the whiskers. (**B**) Example video frame, capturing the silhouette of the whiskers and profile of the mouse face. To track whisking kinematics, the angle (θ) of a whisker (black trace) relative to the mediolateral axis (dotted line) was measured. (**C**) Top, example one second trace of whisker position (θ, black) and its midpoint position (θ_{mid}, *gray*). Middle, whisk amplitude (θ_{amp}) is the half-width, in degrees, of the whisk cycle. Lower bound of scale bar indicates 0°. Bottom, whisk phase (Φ, black), computed for the same trace, is the relative position of the whisker within a whisk cycle. Times when the whisker is in its fully retracted position ($\Phi = \pi$) are indicated by gray lines. (**D**) Schematic illustrating different types of afferents (open circles with dotted lines) recorded in these experiments, grouped by type of receptive field. These include four populations: trigeminal ganglion (TG, beige) low threshold mechanoreceptors (LTMRs) with receptive fields localized to either (1) a mystacial whisker follicle (filled black dots; e.g. black whisker), (2) hairy skin (e.g. gray patch on cheek), or (3) a non-mystacial vibrissa (red dots; e.g. red supraorbital vibrissa), or trigeminal mesencephalic nucleus (MeV) proprioceptors innervating facial muscles. (**E**) Table indicating electrode location (either TG or MeV), number of recorded units, and number of whisking-sensitive units (non-overlapping 95% CI for mean spike rate during whisking vs. non-whisking and >1 Hz mean spike rate during whisking) recorded for each mechanoreceptor group.

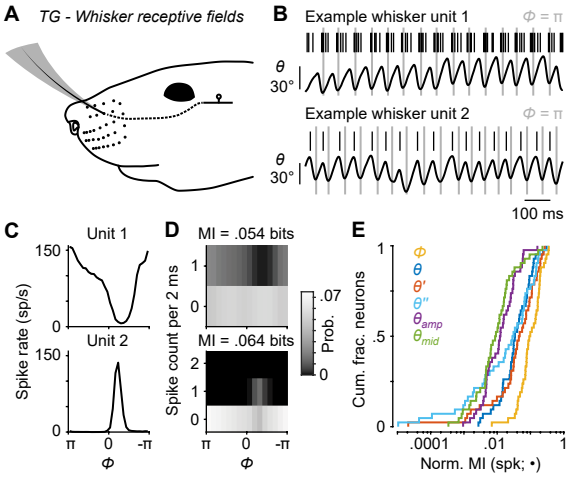

Figure 2. Self-motion responses from mechanoreceptors innervating whisker follicles.
(**A**) Schematic illustrating a unit with receptive field mapped to a whisker follicle (e.g. whisker B2; n = 67 total, 42 whisking-sensitive). (**B**) Spike times (black ticks) for two example whisker afferent units, each aligned with whisker position traces in black (gray lines: fully retracted positions). Unit 1 (top) responded during protracting phases, and unit 2 (bottom) responded during retracting phases. (**C**) Phase tuning curves (mean ± SEM; SEM here and in some subsequent panels narrower than line width) for unit 1 (top) and unit 2 (bottom). (**D**) Joint probability distributions for spike count and whisk phase (Φ), obtained from 2 ms periods corresponding to individual video frames, for unit 1 (top) and unit 2 (bottom). Mutual information (MI) between spike count and phase for each unit is shown at the top of each panel. Per 2 ms period, unit 1 spiked up to once and unit 2 up to twice. (**E**) Cumulative distributions of normalized mutual information values for all whisking-sensitive whisker mechanoreceptors (n = 42), measured between spike count and each kinematic quantity (•): phase (Φ, yellow), position (θ, dark blue), angular velocity (θ', red), angular acceleration (θ'', light blue), whisking amplitude (θ_{amp}, purple), and whisking midpoint (θ_{mid}, green). A subset of whisker afferent recordings was previously reported (Severson et al., 2017) and are reanalyzed here (see Supplemental Table 1 for details).

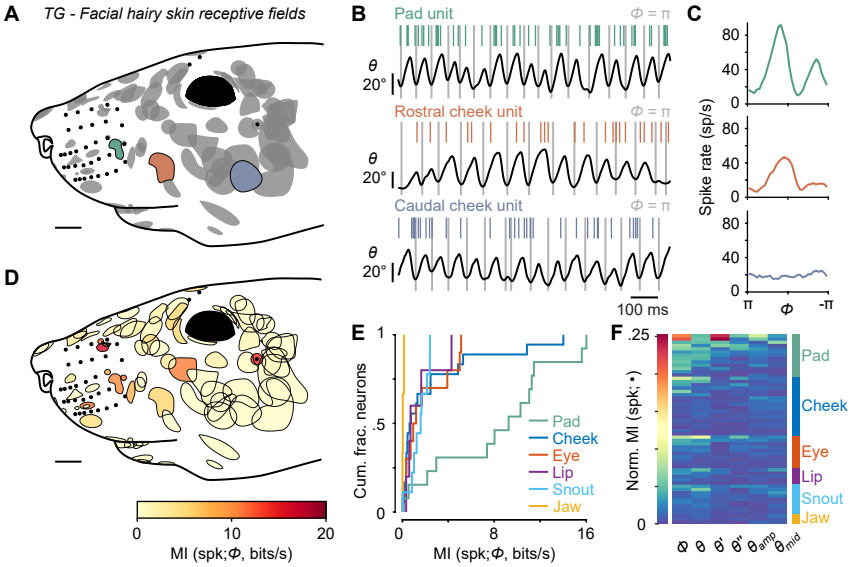

Figure 3. Self-motion responses from mechanoreceptors innervating facial hairy skin.
(**A**) Receptive fields on facial hairy skin (n = 85). Approximate size, shape, and location of receptive fields (gray) were compiled onto a template image of a mouse face (scale bar: 2 mm). Colored receptive fields show examples from whisker pad (green), rostral cheek (orange), and caudal cheek (blue). Whisker follicles and non-mystacial vibrissae (filled black dots) are included as fiducial marks. (**B**) Example one second traces showing spike times (colored ticks) aligned with whisker position (black trace; gray lines: fully retracted positions), from recordings corresponding to the examples in (A). (**C**) Phase tuning curves (mean ± SEM) for example pad unit (green, top), rostral cheek unit (orange, middle), caudal cheek unit (blue, bottom).Example cheek units illustrate that units with similar mean spike rates during whisking can differ in their phase modulation. (**D**) Mutual information (MI; expressed as a rate by multiplying by the sampling frequency of 500 Hz; color scale) between spike count and phase overlaid on outlines of receptive fields (scale bar: 2 mm). Many but not all receptive fields with large MI values were located near whiskers. (**E**) Cumulative distributions of MI rate between spike count and phase for whisking-sensitive neurons with receptive fields in each region of the face, including whisker pad (green, n = 13), cheek (dark blue, n = 18), eye (red, n = 10), lip (purple, n = 5), snout (light blue, n = 9), and jaw (yellow, n = 3). (**F**) Heatmap of normalized MI values for all whisking-sensitive facial hairy skin units (n = 58), measured between spike count and each kinematic quantity (•, columns): phase (Φ), position (θ), angular velocity (θ'), angular acceleration (θ''), amplitude (θ_{amp}), and midpoint (θ_{mid}). Units (rows) are sorted by receptive field location (labeled at right) and within each face region by increasing normalized MI averaged across the kinematic quantities.

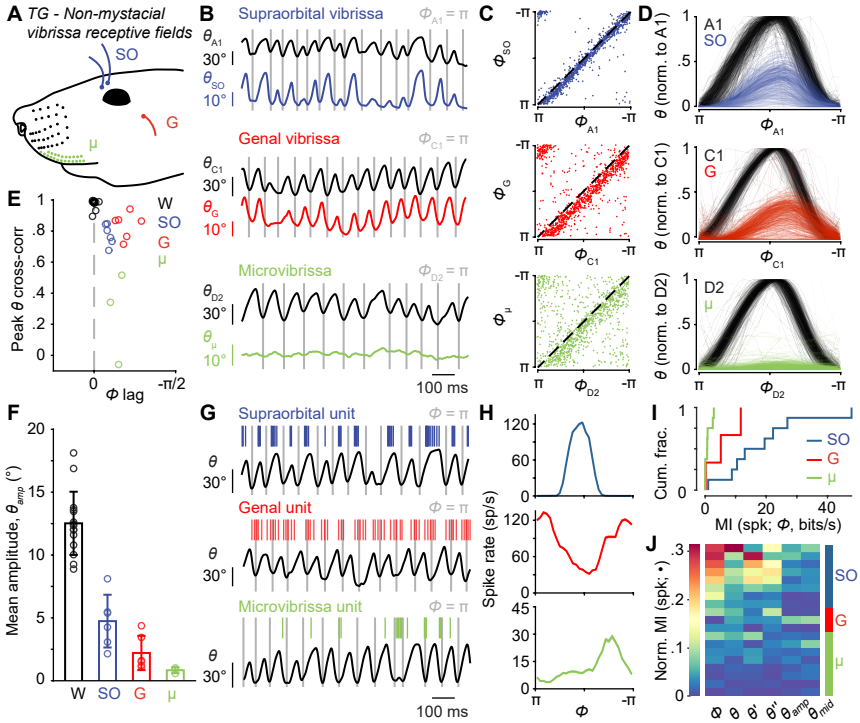

Figure 4. Non-mystacial vibrissae move in phase with whiskers, and their mechanoreceptors encode motion. (**A**) Schematic of non-mystacial vibrissae included in these experiments: supraorbital (SO, blue) above the eye, genal (G, red) on the cheek, and microvibrissae (μ, green) on the upper lip. (**B**) Correlated motion between whiskers and non-mystacial vibrissae. Example one second trace of whisker (black) and vibrissa angle (top, supraorbital, blue; middle, genal, red; bottom, microvibrissa, green) tracked simultaneously (gray lines: fully retracted whisker positions). (**C**) Scatter plot of whisk phase for whisker vs. non-mystacial vibrissae (n = 1000 randomly chosen frames; top, SO, blue; middle, G, red; bottom, μ, green; dashed black lines: unity). (**D**) Trajectories of whisker and non-mystacial vibrissa angles through each whisk cycle, normalized to the whisker angle (n = 500 randomly chosen cycles; top, A1 and SO angle; middle, C1 and G angle; bottom, D2 and μ angle). (**E**) Peak cross-correlation (Pearson's r) and phase lag (open circles) for θ of tracked whisker and either adjacent whisker (W, gray; n = 14 whisker pairs from 12 mice), supraorbital (SO, blue; n = 6 recordings from 6 mice), genal (G, red; n = 6 recordings from 6 mice), or microvibrissa (μ, green; n = 3 recordings from 3 mice). (**F**) Mean whisk amplitude for whisker (W, gray), supraorbital (SO, blue), genal (G, red), or microvibrissa (μ, green). Bars indicate mean ± SD across recordings. (**G**) Example one second periods with spike times from supraorbital unit (top, blue ticks), genal unit (middle, red ticks), and microvibrissa unit (bottom, green ticks) aligned with position of the tracked whisker (θ, black trace; gray lines: fully retracted whisker positions). (**H**) Phase tuning curves (mean ± SEM) for the same examples in (G): top, SO, blue; middle, G, red; bottom, μ, green. (**I**) Cumulative distributions of mutual information rate between spike count and phase of whisking-sensitive neurons with receptive fields on non-mystacial vibrissae, including SO (blue, n = 8), G (red, n = 3), and μ (green, n = 8). (**J**) Heatmap of normalized mutual information for all whisking-sensitive non-mystacial vibrissa units (n = 19), measured between spike count and each kinematic quantity (•, columns): phase (Φ), position (θ), angular velocity (θ'), angular acceleration (θ''), amplitude (θ_{amp}), and midpoint (θ_{mid}). Units (rows) are sorted by receptive field location (labeled at right) and within each non-mystacial whisker by increasing normalized MI averaged across the kinematic quantities.

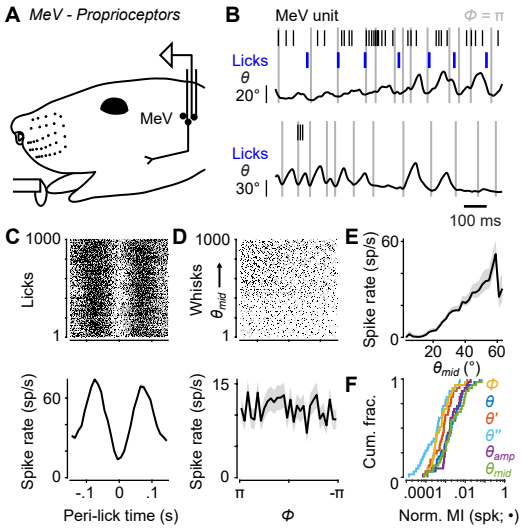

Figure 5. Responses of proprioceptors in the trigeminal mesencephalic nucleus during licking and whisking. (**A**) Schematic of trigeminal mesencephalic nucleus (MeV) electrophysiological and behavioral recordings. Microelectrode drives were implanted into MeV. MeV jaw proprioceptor neurons were identified based on responses to passive jaw stretch and to active jaw movements occurring while licking for water reward. (**B**) Example one second period with MeV unit spike times (black ticks) and lick times (blue ticks) aligned with position (black trace) of the tracked whisker (gray lines: fully retracted positions). (**C**) Top, spike raster aligned to lick times (n = 1000 randomly chosen licks) for example unit in (B). Bottom, peri-event time histogram aligned to lick times (mean ± SEM) for all licks. (**D**) Top, spike raster aligned to whisk cycles (n = 1000 randomly chosen whisks) for unit in (B). Bottom, peri-event time histogram aligned to whisk phase (mean ± SEM) for all whisk cycles. Whisks are ordered by increasing mean θ_{mid}. (**E**) Midpoint (θ_{mid}) tuning curve (mean ± SEM) for unit in (B). (**F**) Cumulative distributions of normalized mutual information for all whisking-sensitive MeV units (n = 33), measured between spike count and each kinematic quantity (•): phase (Φ, yellow), position (θ, dark blue), angular velocity (θ', red), angular acceleration (θ'', light blue), amplitude (θ_{amp}, purple), and midpoint (θ_{mid}, green).

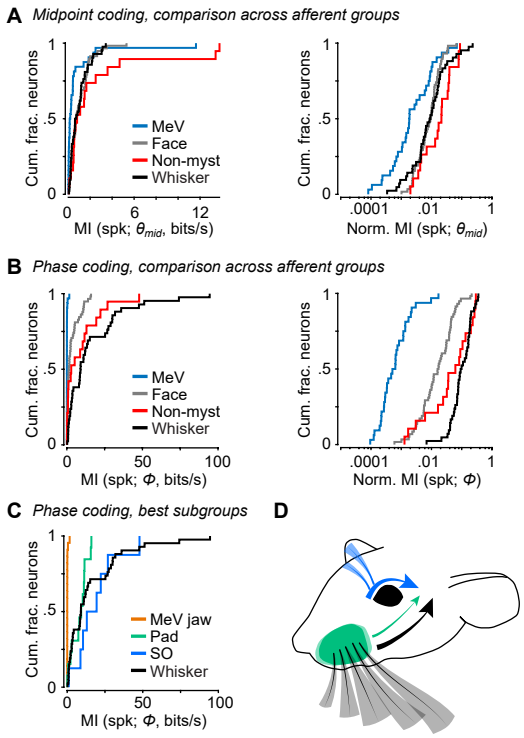

Figure 6. Coding of self-motion by diverse classes of facial mechanoreceptors.
(**A**) Summary cumulative distributions of mutual information rate between spike count and midpoint (θ_{mid}) for whisking-sensitive MeV (blue, n = 33), face (gray, n = 58), non-mystacial vibrissae (red, n = 19), and whisker units (black, n = 42). (**B**) Left, summary cumulative distributions of normalized mutual information between spike count and θ_{mid} for all whisking-sensitive MeV (blue), face (gray), non-mystacial vibrissae (red), and whisker units (black). Right, summary cumulative distributions of MI rate between spike count and phase (Φ) for whisking-sensitive neurons. (**C**) Left, summary cumulative distributions of normalized mutual information between spike count and phase for all whisking-sensitive MeV (blue), face (gray), non-mystacial vibrissae (red), and whisker units (black). Right, summary cumulative distributions of MI rate between spike count and phase for whisking-sensitive jaw proprioceptors (orange, n = 23), whisker pad afferents (green, n = 13), SO afferents (blue, n = 8), or whisker afferents (black, n = 42). Data for pad and SO afferents taken from Figures 2E and 3I, respectively. (**D**) Schematic depicting flow of information about whisking kinematics from various peripheral mechanoreceptors to the brain: whisker follicle afferents (black), supraorbital vibrissa afferents (blue), and whisker pad hairy skin afferents (green). (**B**,**D**) Data are taken from Figures 1-4 and plotted together for comparison.

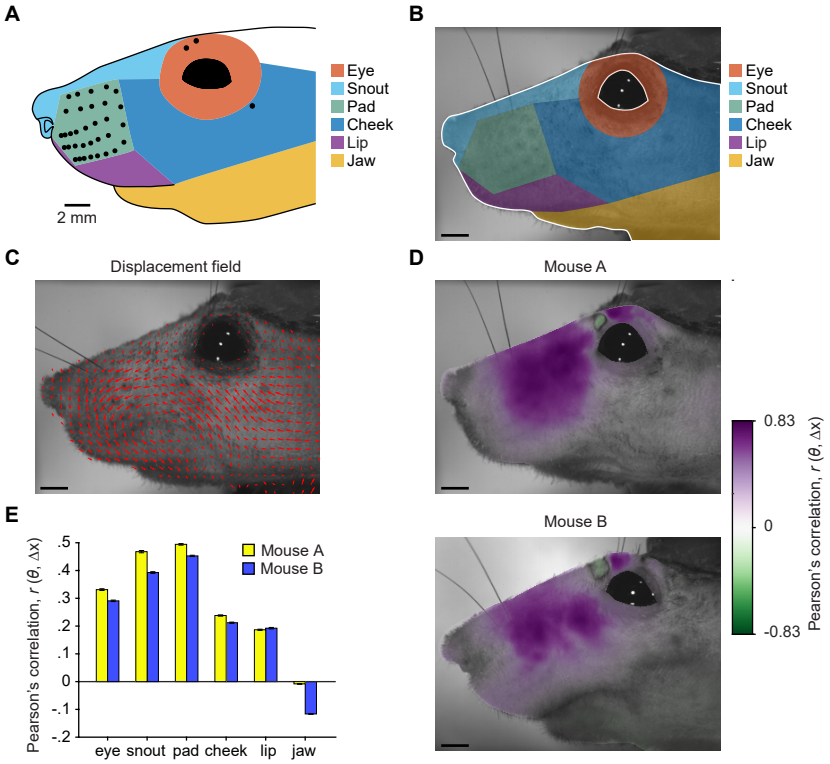

Supplemental Figure 1. Widespread facial movement correlated with whisker motion.
(**A**) Six facial regions on template mouse face were used for categorizing afferent receptive fields. Zones were drawn based on fiducial marks, including the mystacial whiskers (filled circles). Locations of non-mystacial vibrissa follicles (open circles) are also indicated. Receptive fields were scaled to the template image. (**B**) "Fixed" template image for image registration method of tracking facial motion. Overlaid are facial regions drawn using image fiducial marks. Pixels outside the edge of the face and within the eye, outlined in white, were effectively excluded from image registration by setting their values to zero. (**C**) Example "moving" frame overlaid with a subset of the estimated x- and y-displacements, plotted as vectors (red arrows), that would align it to the fixed template image. (**D**) Template images from each of two mice overlaid with color scale showing Pearson's correlation coefficients (r) between the time series of each pixel's x-displacement (Δx) and the A1 whisker position (θ). (**E**) Pearson's r values averaged (± SEM) across all pixels within each facial region, separately for two mice. (**B**-**D**) Scale bars: 2 mm.

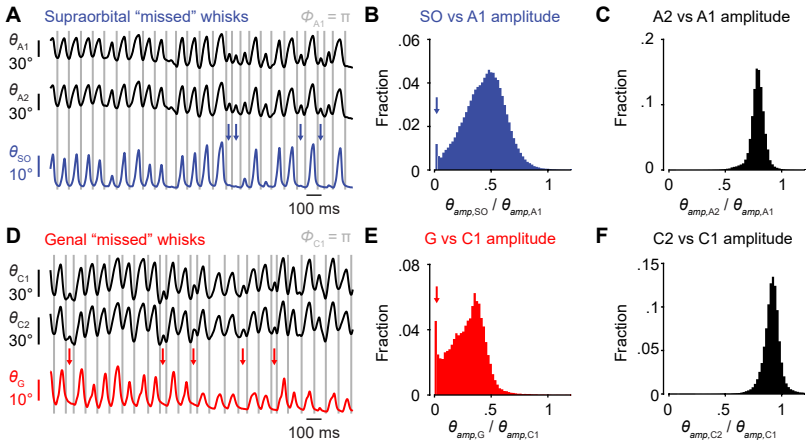

Supplemental Figure 2. Example "missed" whisks by non-mystacial vibrissae.
(**A**) Example traces of simultaneously recorded A1 whisker position (θ_{A1}, top black trace), A2 whisker position (θ_{A2}, bottom black trace) and supraorbital vibrissa position (θ_{SO}, blue; gray lines: fully retracted phase of A1). Whisks by A1 that we not matched by whisks of SO vibrissae (missed whisks) are marked by blue arrows. (**B**) Histogram of ratio of supraorbital vibrissa amplitude ($\theta_{amp,SO}$) over A1 whisker amplitude ($\theta_{amp,A1}$) for whisking periods (330,085 frames) in the example recording in (A). Ratios above 1.2 are not shown on plot for clarity (0.09% of frames). The peak with ratio near zero, indicated by a blue arrow, indicates a substantial fraction of missed whisks in this example recording. (**C**) Same as (B) but for A2 vs A1 whiskers. There is no histogram peak indicative of missed whisks (0.16% of values are above the axis limit of 1.2). (**D**) Example traces of θ_{C1} and θ_{C2} (black traces) and θ_{G} (red; gray lines: fully retracted phase of C1). Missed whisks by the genal vibrissa are marked by red arrows. (**E**) Histogram of ratio of genal vibrissa amplitude ($\theta_{amp,G}$) versus C1 whisker amplitude ($\theta_{amp,C1}$) for whisking periods (96,429 frames) in the example recording in (C). Ratios above 1.2 not shown (0.36% of frames). Missed whisks with amplitude ratio near zero are indicated by the red arrow. (**F**) Same as (E) but for C2 vs C1 whiskers. There is no histogram peak indicative of missed whisks (0.75% of values are above the axis limit of 1.2).

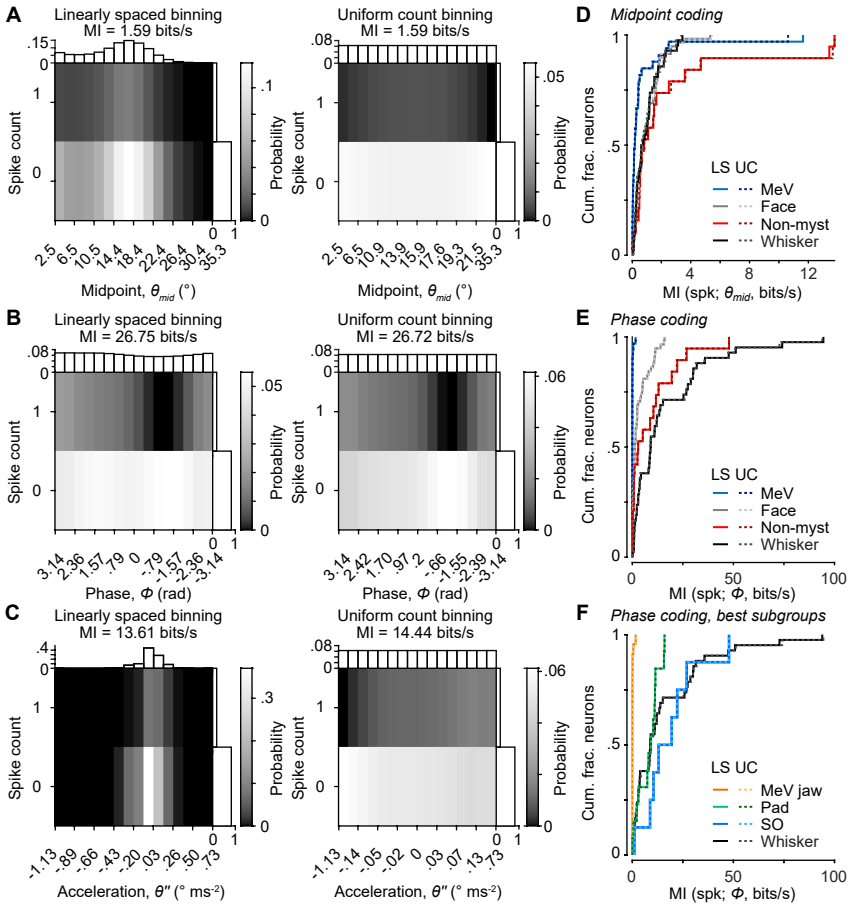

Supplemental Figure 3. Alternative binning methods for mutual information calculation.
(**A**) Joint distribution for spike count and whisk midpoint (θ_{mid}) comparing linearly spaced (left, same calculation reported throughout paper) and uniform count (percentile) binning (right) of θ_{mid} for an example whisker afferent. Note that bin edges are not equally spaced for uniform count binning. Marginal distributions are plotted for θ_{mid} (top) and spike count (right). Mutual information (MI) rate values calculated using each method of binning are reported at the top. (**B**) Joint distribution for spike count and whisk phase (Φ) comparing linearly spaced binning (left) and uniform count binning (right) of Φ for the same example unit. Marginal distributions are plotted on top and to the right. Note that the distribution of phase is almost uniform, except fewer bins are observed during retraction phases due to rapid whisker retraction. MI rate values calculated using each method of binning are reported at top. (**C**) Joint distribution for spike count and angular acceleration (θ'') comparing linearly spaced (left) and uniform count binning (right) of θ'' for the same example unit. Marginal distributions are plotted on top and right. Note that distribution of θ'' has longer tails than θ_{mid} and Φ. MI rate values are reported at top. (**D**) Cumulative distributions of MI rate between spike count and θ_{mid}, calculated using linearly spaced ("LS", solid lines) or uniform count ("UC", dotted lines) binning for the different afferent groups (linearly spaced values are repeated from Figure 6A). (**E**) Cumulative distributions of MI rate between spike count and Φ, calculated using linearly spaced (solid lines) or uniform count (dotted lines) binning for the different afferent groups (linearly spaced values are repeated from Figure 6B). (**F**) Cumulative distributions of MI rate between spike count and Φ, calculated using linearly spaced (solid lines) or uniform count (dotted lines) binning for the best afferent subgroups (linearly spaced values are repeated from Figure 6C).

Mouse ID	Sex	Mouse line	Date of Birth	Recording Dates	Receptive Fields/ Regions of Interest	Unit IDs *prev. incl. in Severson, et al. 2017 ‡ whisking-sensitive	Appearances - Main Figures						Appearances - Supplemental Figures			Other notes
							Fig. 1	Fig. 2	Fig. 3	Fig. 4	Fig. 5	Fig. 6	Fig. S1	Fig. S2	Fig. S3	
Recordings of trigeminal ganglion neurons																
KSt66	M	*TrKC*^{CreER};*Rosa*^{Ai32}	05/09/14	07/11-07/18/14	whisker	125B*, 128D*‡		E				A-C			D-F	
KSt69	M	*TrKC*^{CreER};*Rosa*^{Ai32}	05/09/14	07/28/14	whisker	132A*‡		E				A-C			D-F	
KSt76	M	*TrKC*^{CreER};*Rosa*^{Ai32}	06/29/14	09/27/14	whisker	145B*‡		E				A-C			D-F	
KSt80	F	*TrKC*^{CreER};*Rosa*^{Ai32}	06/29/14	10/25/14	whisker	154B*										
KSt77	M	*TrKC*^{CreER};*Rosa*^{Ai32}	06/29/14	11/10-11/12/14	whisker	161A*‡, 163B*		E				A-C			D-F	
KSt82	M	*TrKC*^{CreER};*Rosa*^{Ai32}	07/20/14	12/08/14	whisker	167A*‡		E				A-C			D-F	
KSt88	M	*TrKC*^{CreER};*Rosa*^{Ai32}	10/28/14	03/20-03/30/15	whisker; micro	194A*; 197C										
KSt89	F	*TrKC*^{CreER};*Rosa*^{Ai32}	10/25/14	03/31/15	whisker	198B*										
KSt92	M	*TrKC*^{CreER};*Rosa*^{Ai32}	10/28/14	04/01-04/05/15	whisker; cheek	202A*; 199A‡			A,D-F			A-B				
KSt91	M	*TrKC*^{CreER};*Rosa*^{Ai32}	10/28/14	04/13/15	whisker	207A*										
KSt96	F	*TrKC*^{CreER};*Rosa*^{Ai32}	01/28/15	04/20/15	whisker	211A*										
KSt94	F	*TrKC*^{CreER};*Rosa*^{Ai32}	10/28/14	04/23-04/24/15	whisker; eye	214A*; 213A‡			A,D-F			A-B			D,E	
KSt95	M	*TrKC*^{CreER};*Rosa*^{Ai32}	10/25/14	04/29/15	whisker; SO	217F*‡; 217A,		E				A-C			D-F	
KSt99	M	*TrKC*^{CreER};*Rosa*^{Ai32}	02/07/15	05/06/15	whisker	220B*‡, 220C*		E				A-C			D-F	
KSt106	F	*TrKC*^{CreER};*Rosa*^{Ai32}	02/07/15	05/08/15	whisker	221B*‡, 221C*		E				A-C			D-F	
KSt101	F	*TrKC*^{CreER};*Rosa*^{Ai32}	02/23/15	05/11/15	whisker	223B*										
KSt107	F	*TrKC*^{CreER};*Rosa*^{Ai32}	02/07/15	05/14-05/15/15	whisker	225D*‡, 227A*‡, 227C*		E				A-C			D-F	
KSt100	M	*TrKC*^{CreER};*Rosa*^{Ai32}	10/25/14	05/18/15	cheek	228A‡			A,D-F			A-B			D,E	
KSt109	F	*TrKC*^{CreER};*Rosa*^{Ai32}	02/07/15	05/21/15	whisker	231A*‡		E				A-C			D-F	
KSt111	M	*TrKC*^{CreER};*Rosa*^{Ai32}	02/07/15	05/29/15	whisker	234A*										
KSt112	M	*TrKC*^{CreER};*Rosa*^{Ai32}	02/07/15	06/06-06/10/15	whisker; micro; G	240A*‡, 243B*; 242B; 242E		E				A-C			D-F	
KSt115	F	*TrKC*^{CreER};*Rosa*^{Ai32}	02/07/15	06/19-06/22/15	whisker; SO	250A*‡; 247A		E				A-C			D-F	
KSt117	M	*CCK*^{Cre}; *Rosa*^{Ai32}	01/03/15	06/29/15	whisker	251B*‡		E				A-C			D-F	
KSt119	M	*TrKC*^{CreER};*Rosa*^{Ai32}	03/25/15	07/02-07/06/15	whisker; cheek; snout	253A*‡, 254C*, 256B*‡; 254A‡; 255B‡		E	A,D-F			A-C			D-F	
KSt122	M	*TrKC*^{CreER};*Rosa*^{Ai32}	03/25/15	07/17-07/19/15	whisker; cheek	265A*; 263A‡			A,D-F			A-B			D,E	
KSt124	F	*TrKC*^{CreER};*Rosa*^{Ai32}	03/25/15	07/21/15	whisker; cheek	266B*; 266A‡			A,D-F			A-B			D,E	
KSt123	F	*TrKC*^{CreER};*Rosa*^{Ai32}	03/25/15	07/25-07/29/15	whisker; cheek; snout; eye	271A*; 268A‡; 270A‡; 270B‡			A,D-F			A-B			D,E	
KSt125	F	*TrKC*^{CreER};*Rosa*^{Ai32}	03/25/15	08/04/15	eye	274A‡			A,D-F			A-B			D,E	
KSm31	M	*TrKC*^{CreER};*Rosa*^{Ai32}	05/10/16	08/20-08/22/16	whisker; eye; pad	275A; 276A‡; 276B‡			A,D-F			A-C			D-F	
KSm30	M	*Rosa*^{Ai32}	05/10/16	08/25-08/26/16	whisker; cheek	278B*‡; 279A‡		E	A,D-F			A-C			D-F	
KSt126	M	*TrKC*^{CreER};*Rosa*^{Ai32}	05/10/16	08/29-08/31/16	whisker; SO	282A*; 280B										
KSt127	F	*TrKC*^{CreER};*Rosa*^{Ai32}	05/10/16	09/07-09/09/16	whisker	285A‡, 286A*‡		E				A-C			D-F	
KSt128	M	*TrKC*^{CreER};*Rosa*^{Ai32}	01/20/16	09/13/16	whisker; pad	288C*‡; 288B‡		E	A,D-F			A-C			D-F	
KSt130	M	*TrKC*^{CreER};*Rosa*^{Ai32}	09/27/15	09/23/16	whisker; cheek	295A*‡; 295B		E	A,D			A-C			D-F	
KSt131	M	*TrKC*^{CreER};*Rosa*^{Ai32}	09/27/15	09/23/16	whisker	295C*‡		E				A-C			D-F	
KSt137	M	*Rosa*^{Ai32}	05/10/16	10/15/16	whisker	303A*‡, 304B*‡, 305B*‡		E				A-C			D-F	
KSt135	M	*TrKC*^{CreER};*Rosa*^{Ai32}	05/10/16	10/24-10/27/16	whisker; snout; pad	309B*‡, 311C*‡; 309A; 311A‡		E	A,D-F			A-C			D-F	
KSt138	M	*TrKC*^{CreER};*Rosa*^{Ai32}	05/10/16	11/20/16	whisker	313A*‡		E				A-C			D-F	
KSt140	M	*TrKC*^{CreER};*Rosa*^{Ai32}	05/10/16	12/01-12/05/16	whisker	318A*‡, 321A*‡, 321B*‡		E				A-C			D-F	
KSt143	M	*TrKC*^{CreER};*Rosa*^{Ai32}	07/04/16	02/17-02/22/17	whisker; snout; eye; pad	332A; 329B, 333B‡; 331A; 332C‡			A,D-F			A-C			D-F	
KSt145	M	*CCK*^{Cre} ; *Rosa*^{Ai32}	07/04/16	02/24-02/28/17	eye; G; micro	335A‡, 338A; 336A‡; 338B‡			A,D-F	I,J		A-B			D,E	
KSt148	F	*TrKC*^{CreER};*Rosa*^{Ai32}	10/24/16	03/02-03/05/17	cheek; eye; pad; micro	341A, 342A; 341B; 341C‡; 343A			A,D-F			A-C			D-F	
KSt147	F	*TrKC*^{CreER};*Rosa*^{Ai32}	10/24/16	03/07-03/08/17	whisker; eye; micro	345B‡; 345A‡, 346A; 346B‡		E	A,D-F	I,J		A-C			D-F	
KSt150	M	*TrKC*^{CreER};*Rosa*^{Ai32}	10/24/16	03/16-03/27/17	whisker; micro; SO; eye; cheek; lip; pad; snout	350C‡; 349A‡, 350D‡; 349B‡; 350A; 350B‡, 352C, 356A‡; 351C‡, 352A‡; 351E‡, 352B‡, 354C‡, 355A‡; 353B‡, 354A, 354B		E	A,D-F	I,J		A-C			D-F	
KSt149	F	*TrKC*^{CreER};*Rosa*^{Ai32}	10/24/16	03/30/17	SO	358A‡				I,J		A-C			D-F	
KSt151	M	*TrKC*^{CreER};*Rosa*^{Ai32}	10/24/16	04/17-04/18/17	micro; jaw; cheek	359A‡; 360A, 363A; 361A, 361E‡, 363B‡			A-F	I,J		A-B			D,E	361E example caudal cheek unit in Fig. 3
KSt152	M	*TrKC*^{CreER};*Rosa*^{Ai32}	10/24/16	04/25-04/28/17	lip; cheek; snout	364A‡, 365A‡; 364B; 367A			A,D-F			A-B			D,E	
KSt155	M	*TrKC*^{CreER};*Rosa*^{Ai32}	12/07/16	07/10-07/17/17	whisker; cheek; jaw; micro; SO; pad	375B‡, 377A‡; 372A; 373A, 373B; 374B; 375C, 376B‡; 376A		E	A,D	I,J		A-C			D-F	
KSt154	M	*TrKC*^{CreER};*Rosa*^{Ai32}	12/07/16	07/20-07/26/17	whisker; jaw	379C, 380A‡; 383A‡		E	A,D-F			A-C			D-F	
KSt157	F	*TrKC*^{CreER};*Rosa*^{Ai32}	12/07/16	08/07-08/12/17	whisker; eye; cheek; jaw	387A, 387C‡; 386A‡; 387B‡, 390B; 390A		B-E	A,D-F			A-C			A-F	387C example unit 2 in Fig. 2 and example in S3
KSt158	F	*TrKC*^{CreER};*Rosa*^{Ai32}	12/07/16	08/16-08/29/17	whisker; jaw; cheek	402A‡; 394A‡, 401A, 401B‡; 394B‡, 395A‡, 397A‡		E	A-F			A-C			D-F	394B example rostral cheek unit in Fig. 3
KSt161	M	*CCK*^{Cre} ; *Rosa*^{Ai32}	07/04/16	09/22-09/25/17	whisker; eye	405A‡,406C‡; 406B‡		E	A,D-F			A-C			D-F	
KSt163	M	*TrKC*^{CreER};*Rosa*^{Ai32}	08/08/17	01/12-01/16/18	SO; snout; pad; lip	408A, 409A, 410B‡, 409B‡, 410A, 411C; 406A‡, 409C‡, 411B‡; 411A‡			A,D-F	I,J		A-C			D-F	
KSt164	M	*Rosa*^{Ai32}	08/08/17	01/29-02/07/18	eye; snout; SO; cheek, pad	415A‡, 420A‡; 416A‡, 420B‡; 416B; 417B‡; 418A‡			A-F			A-C			D-F	418A example pad unit in Fig. 3
KSt166	M	*TrKC*^{CreER};*Rosa*^{Ai32}	08/09/17	02/08-02/16/18	whisker; cheek; snout; SO; G	422C‡, 422D‡; 421B‡, 424A‡; 421C‡, 421D‡; 422A, 422B‡, 424B, 425A‡, 425D; 425C	C,D	B-E	A,D-F	I,J		A-C			D-F	422D example unit 2 in Fig. 2
KSt165	F	*TrKC*^{CreER};*Rosa*^{Ai32}	08/09/17	02/20-02/21/18	G	427A, 428B										
KSt167	F	*TrKC*^{CreER};*Rosa*^{Ai32}	08/09/17	02/24/18	G	430A‡, 430B, 430C				I,J		A-B			D,E	
Recordings of trigeminal mesencephalic nucleus neurons																
HYLC44	M	*TH*^{Cre};*Rosa*^{Ai32}	12/07/15	05/24-05/30/16	MeV	44B-2‡,3‡,4‡; 44C-15‡,16‡					B-F	A-C			D-F	HY44C-15 example in Fig. 5
HYLC46	M	*DBH*^{Cre};*Rosa*^{Ai32}	12/30/15	06/08/16	MeV	46A-6‡,7‡					F	A-C			D-F	
HYLC48	M	*DBH*^{Cre};*Rosa*^{Ai32}	01/10/16	08/17/16	MeV	48D-5‡,6‡,7‡,8‡					F	A-C			D-F	
HYLC52	M	*DBH*^{Cre};*Rosa*^{Ai32}	05/12/16	08/31/16	MeV	52A-16‡,17,18‡					F	A-C			D-F	
HYLC53	M	*DBH*^{Cre};*Rosa*^{Ai32}	05/12/16	09/02/16	MeV	53A-9‡,22‡,23‡,24,25‡,26					F	A-C			D-F	
HYLC55	M	*DBH*^{Cre};*Rosa*^{Ai32}	06/06/16	09/16/16	MeV	55A-3‡,4‡,5‡,6,7,8‡,9‡, 10‡,11‡,12‡,13,14‡,19‡,20					F	A-C			D-F	
HYLC56	M	*DBH*^{Cre};*Rosa*^{Ai32}	06/06/16	09/26/16	MeV	56A-5‡,6,7‡,8‡,12‡,13‡,14,15‡,16					F	A-C			D-F	
Recordings of facial and whisker movement																
KSt159	F	*TrKC*^{CreER};*Rosa*^{Ai32}	12/07/16	10/20/17	SO; face; whisker	*N.A.*				E,F			D,E			
KSt160	M	*TrKC*^{CreER};*Rosa*^{Ai32}	12/07/16	10/14, 10/20/17	SO; whisker	*N.A.*				E,F						face video registration failed
KSt164	M	*TrKC*^{CreER};*Rosa*^{Ai32}	08/08/17	11/08/17	G; SO; face; whisker	*N.A.*				B-F			B-E			
KSt165	F	*TrKC*^{CreER};*Rosa*^{Ai32}	08/09/17	02/20/18	G; whisker	*N.A.*				B-F				D-F		
KSt166	M	*TrKC*^{CreER};*Rosa*^{Ai32}	08/09/17	02/09/18	G; whisker	*N.A.*				E,F						
KSt167	F	*TrKC*^{CreER};*Rosa*^{Ai32}	08/09/17	02/24/18	G; whisker	*N.A.*				E,F						
KSt168	F	*TrKC*^{CreER};*Rosa*^{Ai32}	08/09/17	05/04, 05/06/18	SO; micro; whisker	*N.A.*				E,F						
KSt169	F	*TrKC*^{CreER};*Rosa*^{Ai32}	08/09/17	05/05, 05/06/18	SO; micro; whisker	*N.A.*				B-F				A-C		
KSt170	M	*Ret*^{CreER};*Rosa*^{Ai32}	12/05/17	05/05, 05/06/18	SO; micro; whisker	*N.A.*				E,F						

Supplemental Table 1: Meta-data and mouse information